Energy & Environmental Science

Dynamic Article Links ▶

PERSPECTIVE

Morphology of all-polymer solar cells

Christopher R. McNeill*

The blending of two semiconducting polymers with offset energy levels enables efficient charge generation in thin-film 'all-polymer' solar cells. A key requirement for efficient charge separation and collection is the formation of interconnected phase-separated domains structured on the sub-20 nm length-scale. This review provides an overview of recent advances in the characterisation of conjugated polymer blend nanostructure and developments in the linking of blend structure and device performance. This review also provides a general introduction to the polymer physics behind phase separation, experimental techniques used for characterising blend structure and novel ways to control nanomorphology.

1. Introduction

Semiconducting polymers have a number of properties that make them appealing for use as the active layer in thin-film solar cells. Their high extinction co-efficients enable efficient absorption with 100–200 nm thick films. They are solution processable at room temperature enabling low-cost high-throughput printing of modules.[1] The flexibility afforded by organic synthesis provides large scope for the tuning of optical and electronic properties. Polymer solar cells, however, are still an emerging photovoltaic technology. While they possess lower power conversion efficiencies than established technologies, steady progress has been made over the last ten years increasing the efficiency from a few %[2] to over 8%.[3] Cell stability is also a potential issue for polymer solar cells, however a recent report of cell lifetimes of over 7 years has been encouraging.[4]

Important work still remains in understanding the operation of polymer solar cells and identifying key loss mechanisms. Semiconducting polymers behave significantly differently to

Department of Materials Engineering, Monash University, Wellington Road, Clayton, Victoria, 3800, Australia. E-mail: christopher.mcneill@ monash.edu

inorganic semiconductors, with different processes governing device operation.[5] Consequently polymer solar cells require a blend of two materials in order to facilitate efficient device operation, with the complicated nature of the blend morphology complicating understanding and optimising of device operation.

Polymer solar cells come in a number of flavours, depending on the nature of the two materials used in the active layer blend. In order for charges to be generated, the initial, tightly-bound neutral state that is the primary product of polymer photoexcitation must be dissociated. The dissociation of these excitons is efficient at the interface between materials with different electron affinity and/or ionisation potential, see Fig. 1. Exciton dissociation may proceed either by electron transfer to a material with higher electron affinity, or *via* hole transfer to a material with lower ionisation potential. A range of electron-accepting materials (materials with high electron affinity) have been used in combination with electron donating polymers in polymer solar cells, including fullerene derivatives[6] and inorganic nanoparticles.[7] Two different semiconducting polymers with offset energy levels may also be used,[8] with the morphology of so-called all-polymer solar cells the topic of interest here. The efficiency of all-polymer solar cells has lagged behind that of polymer/fullerene and polymer/nanocrystal solar cells with polymer/fullerene

---

Broader context

As one class of organic solar cell, all-polymer blends have lagged the performance of other types of organic solar cells particularly those based on polymer/fullerene blends. As the nanomorphology of the active blend layer in polymer solar cells is vitally important in determining device efficiency, it is critical to be able to characterise blend morphology with high chemical specificity and spatial resolution. Recent advances in characterisation have provided new insight into the morphology of all-polymer blends underscoring the difficulty in being able to achieve 'ideal' nanomorphologies through solution processing and annealing. In light of the sub-optimal morphology of all-polymer blends, there is scope for engineering of interface and domain structure to enable efficiency improvements. Novel processing routes such as nano-imprint lithography and the application of block co-polymers are promising strategies with recent results providing proof of concept.

---

efficiencies surpassing 8%,[3] polymer/nanocrystal efficiencies surpassing 3%[9] compared to best all-polymer efficiencies of only ∼2%.[10–12] The origin of this lower efficiently is not entirely clear, with a number of factors including poor charge separation,[13] low charge carrier mobilities[14] and sub-optimal morphologies[15] all potentially playing a role. All-polymer solar cells do, however, have a number of potential advantages over polymer/fullerene and polymer/nanocrystal solar cells such as higher open-circuit voltages and improved opportunity for covering complementary regions of the solar spectrum.

This perspective focuses on the nature of the nanoscale morphology of all-polymer solar cells and considers its role in limiting the device performance of this class of device. A consideration of the morphology of all-polymer blends as distinct to polymer/fullerene blend is warranted not only because of the differences in the polymer physics concerning polymer/polymer mixtures compared to polymer/small molecule mixtures, but also due to the unique opportunities afforded by polymers for controlling nanomorphology. This perspective will, however, cover areas of interest to the general organic photovoltaics community including discussion of techniques for characterising blend morphology and routes to control nanomorphology such as the use of block-copolymers.

After introducing the basic operating mechanisms of polymer solar cells, a brief discussion of the thermodynamics of phase separation in polymer blends will be presented. An overview of the experimental techniques for characterising blend morphology will then be discussed, highlighting the need for techniques with high spatial resolution and high chemical specificity. Discussion will then turn to our current understanding of the nature of polymer blend thin-film morphology and its relation to device performance. Finally novel routes for control of morphology afforded by polymers will be discussed and the potential for such morphological control to drive efficiency improvements.

Chris McNeill is a Senior Lecturer in the Department of Materials Engineering at Monash University, Melbourne Australia. After graduating in 2005 with a PhD in physics from the University of Newcastle, Australia, he joined the optoelectronics group at the Cavendish Laboratory, University of Cambridge. There he continued to study the relationship between device operation and microstructure in organic semiconductor devices, pioneering the use of soft X-ray techniques such as X-ray spectromicroscopy in this field. In 2007 he was awarded an EPSRC Advanced Research Fellowship enabling him to establish his own research portfolio. In 2011 he returned to Australia to establish an organic electronics research group, supported by the award of an ARC Future Fellowship and VESKI Innovation Fellowship.
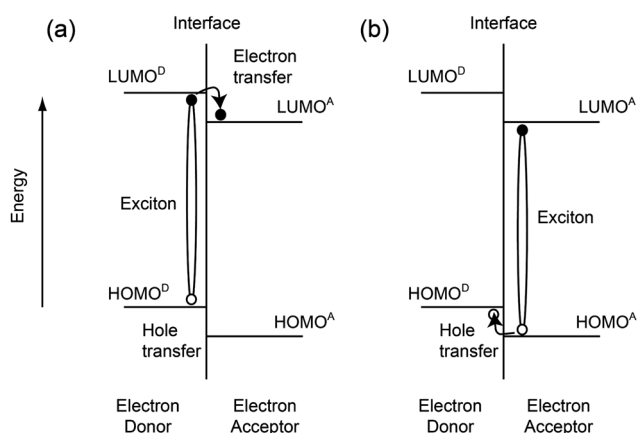
Christopher R. McNeill

Fig. 1 Schematic diagram showing energy level offsets and charge transfer processes at a donor/acceptor heterojunction. The lowest unoccupied molecular orbital (LUMO) and highest occupied molecular orbital (HOMO) of donor (D) and acceptor (A) are labelled. The polymer with the deeper LUMO (high electron affinity) acts as the electron acceptor while the polymer with shallower LUMO (lower electron affinity) acts as the electron donor. Excitons in the donor phase are dissociated by electron transfer, (a), at the donor/acceptor interface while excitons in the acceptor phase are dissociated by hole transfer, (b), at the donor/acceptor interface.

2. Operation of polymer solar cells

As mentioned above, free charges are not the primary product of photoexcitation in semiconducting polymers but instead neutral excitons (that can be thought of bound electron-hole pairs) are predominantly formed.[5] While excitons are known in inorganic semiconductors, due to the particular properties of organic semiconductors, such as low dielectric constants and strong electron–phonon coupling, the binding energy of excitons in organic semiconductors is relatively large, ∼0.4 eV.[5] Thus thermal energy or built-in fields are not sufficient to dissociate these excitons into charges. Instead exciton dissociation relies upon the diffusion of excitons to an interface between two different materials with offset energy levels. With reference to Fig. 1, the material with the higher electron affinity or deeper LUMO (lowest-unoccupied molecular orbital) is known as the electron acceptor (or simply as the acceptor) and the material with the lower electron affinity or shallower LUMO the electron donor.

The simplest donor/acceptor polymer solar cell geometry consists of a bilayer of donor and acceptor layers sandwiched between two planar electrodes, see Fig. 2a. Indium-tin oxide (ITO)-coated glass typically serves as the high work function
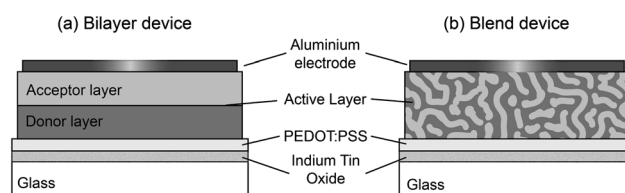

Fig. 2 Schematic diagram of the geometry of typical bilayer (a) and blend (b) polymer photovoltaic devices. In the active layer the dark regions represent the electron donating polymer and the lighter regions represent the electron accepting layer.

transparent electrode with a top low work function metal electrode completing the device. Due to the low exciton diffusion length, typically 10 nm or less,[16] the use of polymer layers thick enough to enable effective light absorption (50–100 nm thick) means that bilayer devices are limited by the small fraction of excitons that are able to reach the donor/acceptor interface. The blending of two materials to form an active layer with donor/acceptor interfaces distributed throughout the film, see Fig. 2b, enables effective light absorption while maintaining efficient charge generation. This bulk-heterojunction concept as it is known was reported simultaneously for all-polymer blends and polymer/fullerene blends in the mid 1990s.[17–19]

Once an exciton has been dissociated at a donor/acceptor interface, the resulting electron and hole formed are not necessarily free. Due to the low dielectric constant of organic semiconductors ($\varepsilon_r \sim 3$–4) this geminate electron-hole pair must overcome their mutual Coulomb attraction in order to separate from the interface and avoid geminate recombination.[5] There is currently much debate in the literature as to the nature of charge separation in organic solar cells in general, and the potential role played by electric fields,[20,21] excess thermal energy[22,23] and interface dipoles[24,25] in enabling charge separation and hence efficient device operation. The geminate recombination of interfacial electron-hole pairs in particular is often cited as the primary reason for the low efficiency of all-polymer solar cells[26–28] compared to polymer/fullerene cells.

Following the successful separation of electron and hole from the donor/acceptor interface, charges must be able to reach the device electrodes, facilitated by percolation pathways of donor and acceptor materials. Low charge carrier mobilities can lead to the build-up of charge in the device enhancing the probability of bimolecular charge recombination.[5] Although organic semiconductors general possess lower mobilities than inorganic semiconductors, the thin active layer (typically 100–200 nm) employed in organic solar cells means that charge extraction can still be efficient despite these low carrier mobilities. Phase-separated, pure domains can also reduce the probability of bimolecular recombination as electrons and holes are constrained to separate phases.[29]

Much is therefore required of the nanostructured bulk heterojunction morphology to enable efficient device operation, and this of structures typically produced by the natural phase separation during solution-deposition. Domains should have a characteristic spacing less than the exciton diffusion length in order to maximise charge generation via exciton dissociation, however these domains must be interconnected allowing charge transport to the electrodes without 'dead-ends' that result in the build-up of space charge. Device simulations have been very useful in enabling the relationship between device performance and morphology to be studied in a controlled environment. Fig. 3 presents the results of simulations using computer-generated morphologies to study how device performance varies as the blend morphology is allowed to evolve.[30] Three morphologies are pictured with different degrees of phase separation that have been generated by minimization of the Ising Hamiltonian. The bottom graph in Fig. 3 plots the evolution of exciton dissociation efficiency, charge collection efficiency and internal quantum efficiency as a function of interfacial area. While the exciton dissociation efficiency systematically decreases as the
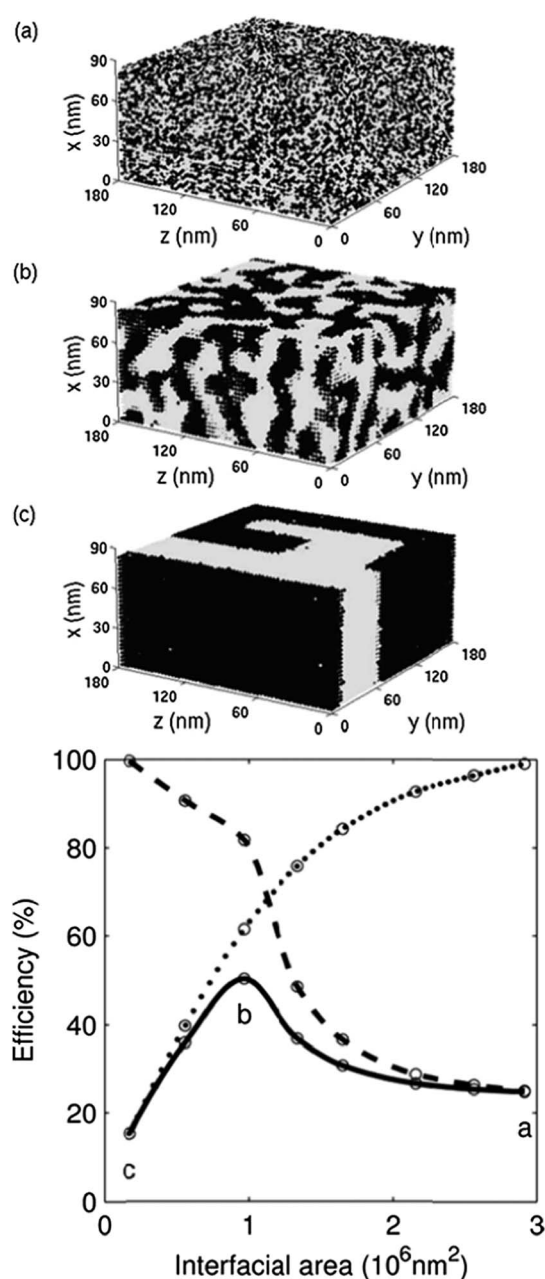

Fig. 3 Top: three example morphologies generated by minimization of the Ising Hamiltonian with electron donating and electron accepting phases depicted by light and dark shades, respectively. Bottom: Plots of the exciton dissociation efficiency (dotted line), charge collection efficiency (dashed line), and internal quantum efficiency (solid line) vs. interfacial area. Reprinted with permission from ref. 30. Copyright 2005 American Chemical Society.

morphology evolves, charge collection efficiency systematically increases with the optimum internal quantum efficiency found for an intermediate morphology that balances the requirements of charge generation and charge collection. Groves et al.[31] have also used simulated morphologies to study the interaction between domain size and device performance, highlighting the connection between domain size and charge separation efficiency. While it was shown that in a bilayer geminate pairs become effectively free when separated from the bilayer interface

by ~4 nm, in a blend the geminate separation efficiency was observe to improve continuously as the average domain size was increased from 4 nm to 16 nm. The reason behind this apparent discrepancy between bilayer and blend is the fact that a restricted blend morphology can reduce the number of possible routes to further separation[32] making charge pairs in blends more susceptible to recombination than charge pairs in a bilayer.

As helpful as these simulations are, the morphologies simulated do not necessarily resemble the actual morphologies of solution-processed thin-film blends. The cartoon blend structure of Fig. 2b is also misleading, belying an expectation/desire of pure phases, sharp interfaces and domains with well-defined domain size. In real-world morphologies one may expect and indeed one encounters impure domains, diffuse interfaces and a hierarchy/broad distribution of domain sizes. Before discussing the structure of real-world blends it is useful to briefly consider the polymer physics behind phase separation.

3. Thermodynamics of phase separation

Whether the blending of two polymers leads to a single, intimately mixed phase or to phase separation into two compositionally distinct phases depends on the interplay between the entropy and enthalpy of mixing. Due to the increased disorder of a mixed system, from entropic considerations an intimately mixed phase of two materials is favoured over discrete phases. However, in the absence of specific interactions between the two different polymer species, it is generally energetically favourable for each polymer to interact with its own kind, favouring phase separation. Whether it is energetically favourable for a system to phase separate is determined by the free energy of the mixture defined as

$$F_{mix} = F_{A+B} - (F_A + F_B) \quad (1)$$

where $F_A + F_B$ is the total free energy of the separated system and F_{A+B} is the free energy of the single, intimately mixed phase. Due to the complexity of polymer systems an exact theoretical treatment is prohibitive requiring approximate treatments or simulations. The most well-known theoretical treatment is the mean-field approach of Flory and Huggins which derives the following expression for the free energy of mixing:[33]

$$\frac{F_{mix}}{kT} = \frac{\phi_A}{N_A}\ln(\phi_A) + \frac{\phi_B}{N_B}\ln(\phi_B) + \chi\phi_A\phi_B \quad (2)$$

Here $\varphi_{A/B}$ is the composition of polymer A/B (with $\varphi_A + \varphi_B = 1$), $N_{A/B}$ is the degree of polymerization of polymer A/B and χ is the Flory-Huggins interaction parameter. The first two terms on the right hand side of (2) relate to the entropy of mixing per monomer unit, while the last term is the enthalpic component. From the entropic terms it can be seen that the translational entropy associated with each chain is reduced by a factor N to reflect that monomers in the same chain are connected and cannot be positioned independently. Thus compared to small molecule mixtures the entropy of mixing is small and the entropic force driving polymer miscibility is weak. Regarding the enthalpic component, the interaction parameter χ in principle may be positive or negative. A negative value of χ corresponds to fully miscible polymer pairs usually the result of specific chemical
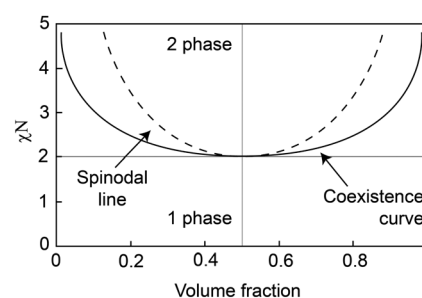

Fig. 4 Flory-Huggins phase diagram for a 2-component polymer blend for components with equal degrees of polymerisation.

interactions, though in the vast majority of cases χ is positive. For the case of $N_A = N_B$ solutions to (2) only exist for values of χ greater than $2/N$, with phase separation energetically favourable for all values of χ greater than $2/N$.[33] Fig. 4 presents the phase diagram for the Flory-Huggins model with components of equal degrees of polymerisation. The co-existence curve separates the one-phase region from the two-phase region. Within the two-phase side of the co-existence curve two different cases may be distinguished: those that are stable and those that are unstable to small composition fluctuations, separated by the spinodal line. Although for all points in the two-phase region of the phase diagram phase separation is energetically preferred, there are metastable regions where the system is locally stable with respect to small composition fluctuations. Within these metastable regions an energy barrier must be overcome in order to achieve the global energy minimum. On the unstable side of the spinodal line, any small fluctuation in composition leads to the lowering of the free energy with phase separation proceeding spontaneously and uniformly throughout the material *via* the amplification of random composition fluctuations, referred to as spinodal decomposition. In the metastable region a small composition fluctuation actually raises the free energy and in order for the phase-separation process to be initiated a droplet of the minority phase of sufficient size has to be nucleated (nucleation and growth).

Since the deposition of the active polymer blend layer in a polymer solar cell is *via* solution deposition, the problem becomes a three-phase rather than two-phase one. In solution, the solvent molecules dilute the polymer/polymer interactions and the system forms a single phase. During film deposition solvent evaporates and as the solvent concentration decreases the interactions between polymer chains increase, increasing the driving force for phase separation. As the solvent concentration decreases, however, the polymer chains become less mobile and once a glass transition is encountered the morphology is frozen in. This frozen-in morphology is generally a non-equilibrium morphology due to the rapid evaporation of solvent as is typically encountered during spin-coating. These frozen morphologies may be unstable to further phase separation with swelling of the film with solvent vapour or heating above the glass transition used to evolve the morphology further. Note that in the simple Flory-Huggins model phase separation actually takes place as the temperature is lowered, with polymer miscibility increasing with increasing temperature. In many systems, as shown below, phase separation is observed as the temperature is raised. This is a reflection that either the interaction parameter

has a different temperature dependence to the Flory-Huggins picture, or that heating above the glass transition unfreezes the system enabling phase separation to proceed.

During the solution deposition of thin films the film interfaces (ie the substrate/film and film/air interfaces) often play an important role in influencing the structure of the film. Following sufficient solvent evaporation such that the system enters the two-phase region of the phase diagram, phase separation between solution phases rich in one of the two polymers is initiated. A layer of one phase often forms at the film/air surface either due to the growth of a wetting layer or the process of surface-directed spinodal composition.[33] Due to rapid solvent evaporation, the composition of solvent throughout the film will be non uniform further promoting layering. Wetting layers in thin-film polymer blends are common, with vertical phase separation leading to the formation of discrete bilayers in extreme cases.[34] Lateral and vertical phase separation are often observed together in the same film.[35,36] Moreover, Heriot and Jones[37] have shown that lateral phase-separation in spin-coated films may actually proceed via an initial, transient wetting layer. Under this mechanism, the film first separates into two layers, followed by an instability of the polymer/polymer interface that grows until the magnitude of the instability is such that this internal liquid/liquid interface meets the surface, at which point the film laterally phase separates.[37]

In light of the complexity of phase separation in solution-processed thin-film polymer blends, the challenge of creating an 'ideal' morphology of a nanostructured thin film with interpenetrating networks of domains with characteristic spacing of ~10 nm is a daunting one. In order to achieve domains of such size, the coarsening of phase separation must be arrested as equilibrium morphologies typically have a much larger domain size. The use of frozen morphologies, however, is not ideal from an ageing perspective, since non-equilibrium morphologies will tend to slowly evolve over time (especially over the lifetime of a solar cell). Furthermore given that sharp interfaces rather than diffuse ones result in higher charge separation efficiencies (see discussion below) a non-equilibrium, finely-mixed morphology will typically have a non-ideal interface structure as the interface width decreases with increasing domain size.[33] Thus optimised morphologies produced via arrested phase separation may never achieve ideal structures due to the non-ideal nature of the interfaces. Little regard is generally given to the nature of polymer/polymer interfaces in all-polymer solar cells despite the importance of donor/acceptor interfaces in device operation. The use of (semi-)crystalline polymers may provide a route to shaper interfaces, however crystallisation processes complicate phase separation further. In principle the use of crystalline polymers may help to naturally arrest phase separation due to the formation of crystallites of well-defined size, however the size of these crystallites must also match the desired length-scales for optimum device operation. The majority of crystalline conjugated polymers however are semi-crystalline, with the presence of both amorphous and crystalline components complicating the phase behaviour further.

Experimentally, the morphology of thin-film photovoltaic polymer blends is varied through the use of different solvents,[38] annealing,[27] varying molecular weight,[39] solvent additives/mixtures[12,40] and solvent annealing.[41] Each of these approaches enables an aspect of the morphology produced to be tuned, but none of these approaches enables full control over the film microstructure. The use of different solvents provides a handle for tuning the degree of phase separation produced by varying the film drying time via the use of solvents with different volatilities. Changing solvent however, can also lead to changes in polymer solubility. Once a film is produced, thermal annealing is a common approach to enable coarsening of phase separation by heating above the glass transition of one or both components enabling the morphology to evolve. It is generally more convenient to alter the annealing temperature while fixing the annealing time, rather than varying the annealing time and fixing the annealing temperature, however it must be noted that polymer miscibility increases with increasing temperature and these two approaches are not therefore not necessarily equivalent. A more natural way to tune morphology is by exposing a deposited film to solvent vapour, or by tuning the film drying time by either spin-coating in a solvent-rich atmosphere or using co-solvents. The use of co-solvents to tune morphology has become popular in recent years, especially in polymer/fullerene blends.[42] The use of a high boiling point co-solvent of variable concentration in a solution where a low boiling point solvent is the majority component enables a convenient tuning of film drying time. Co-solvents can also be judiciously chosen to solubilise one component but not the other to enable the packing of this phase to be optimised without coarsening the morphology further.

4. Characterisation of polymer blend morphology

Characterising the morphology of thin-film polymer blends with high chemical specificity and spatial resolution is a challenging endeavour.[43] While often what is of most interest it the characteristic domain size (though of course there may not be a single or any characteristic domain size) full characterisation of morphology also requires a characterisation of surface composition and interface structure. For blends with semi-crystalline polymers characterisation of crystallinity, crystallite size and orientation is also important. No single technique is able to fully characterise the morphology of a thin-film polymer blend requiring the use of complementary techniques. Similar challenges are faced characterising the domain structure of neat polycrystalline films used in organic field-effect transistors and the reader is directed to a recent review by the author providing complementary discussion on this topic.[8]

The most common tool for characterising polymer blends in the field of organic photovoltaics is atomic force microscopy (AFM).[2,11,44,45] While AFM enables imaging of surface topography with high spatial resolution (≤10 nm) using a lab-based instrument, distinguishing regions with different composition is difficult. Moreover, due to the fact that surface wetting layers are almost always observed,[36,46] AFM characterisation generally reveals information about this surface-rich layer providing little information regarding bulk nanostructure.

The use of photoluminescence quenching measurements is also a common lab-based tool for inferring information about film structure.[27,28,44] Due to the limited exciton diffusion length, efficient photoluminescence quenching implies that donor and acceptor polymers are mixed on the sub-10 nm length scale. Furthermore, with modelling, photoluminescence data can be

used to infer information regarding domain sizes.[27,47] However photoluminescence measurements cannot easily distinguish well-mixed, pure domains from large domains with a minority component that still serve to efficiently dissociate excitons. The length scales that can be probed with photoluminescence measurements are also limited to the exciton diffusion length. Photoluminescence measurements additionally rely on at least one of the components being sufficiently luminescent, which is not always the case.

Transmission electron microscopy (TEM) is able visualise bulk structure with very high resolution (1 nm or less).[48] TEM is particularly suited to studying organic photovoltaic blends since the active layer thickness is sufficiently thin. Similar to AFM, distinguishing different phases can be difficult due to the similar electron densities of different polymers. Defocusing of the electron beam is often used to provide increased contrast however this may lead to artefacts. Staining can be used to increase contrast if a suitable staining agent can be found that specifically binds to one polymer but not the other, see Fig. 5. Increased chemical contrast is also afforded with energy-filtered TEM.[49,50] Here, the chemical composition of the sample is measured by analyzing the electron energy loss spectrum of (inelastically scattered) electrons passing through the sample in the TEM experiment.[43,49] Detecting transmitted electrons with an energy loss characteristic of a specific atomic core level, quantitative two-dimensional elemental distribution maps can be obtained with nanometre resolution and high chemical accuracy.[49]

The use of tuneable soft X-rays at a synchrotron also affords high chemical contrast due to differences in the near-edge X-ray absorption fine structure (NEXAFS) spectra of different conjugated polymers.[51,52] In addition to elemental sensitivity afforded by tuning to the ionisation edge of different constituent atoms, excellent chemical sensitivity can be achieved for polymers with identical chemical composition by tuning to different molecular resonances at the carbon K-edge that are characteristic of each material. Although the resolution of scanning transmission X-ray microscopy (STXM), 25 nm, is not as good as TEM the chemical contrast is arguably better. Examples STXM images are provided in section 5 below.

An inherent limitation in the use of transmission microscopies such as TEM and STXM is the fact that what is imaged is a two-dimensional projection of a three-dimensional structure. The use of electron[53] or X-ray tomography[54] are exciting developments that enable direct visualisation of three-dimensional nanostructure although they involve many projections taken at different angles (requiring samples to be stable to prolonged electron and X-ray radiation) and complicated reconstructions.

Scattering experiments are a complementary alternative to real-space imaging. In a scattering experiment the scattering intensity is measured as a function of the scattering vector q, with inversion of such scattering profiles providing information about the size of scattering features. Small angle-neutron scattering (SANS) has been well-used historically for the study of polymer blends in general and is increasingly being applied to study the structure of photovoltaic polymer blends.[55–57] Deuteration of one polymer is typically required to provide sufficient scattering contrast and the low scattering intensity from thin films can be an issue. For polymer/fullerene blends a high neutron scattering contrast naturally exists between polymers and fullerene-based acceptors making this technique particularly attractive. X-rays are also used for scattering experiments, with hard X-ray scattering experiments an invaluable tool for probing material crystallinity, crystallite size and orientation. A recent advance has been the development of resonant soft X-ray scattering (R-SoXS).[15,58,59] In contrast to hard X-rays that scatter predominantly from atomic cores, the same contrast mechanism employed in STXM allows for the size of compositionally distinguishable domains to be measured with sub-10 nm resolution with R-SoXS, see Fig. 9 in section 5 below.

Due to the layering of thin films that occurs during film deposition (such as via surface-directed spinodal decomposition) it is important to characterise the vertical composition gradient. Surface-sensitive techniques such as X-ray photoelectron spectroscopy (XPS) and electron yield NEXAFS spectroscopy can provide information about surface composition with high accuracy. Depth-profiles can be achieved with nuclear reaction analysis that is able to directly measure the composition of a blend as a function of depth within the film,[35,60] see Fig. 6, or by techniques that etch through the film characterising the composition of the exposed layers with surface sensitive techniques such as XPS[61] or through the use of secondary ion mass spectrometry.[62]

With regard to interface structure, techniques are required that have sensitivity to compositional profiles across polymer/polymer interfaces. The characterisation of interface widths within thin-film blends is extremely challenging, however bilayers may be used as model systems enabling the use of reflectivity experiments. Here a collimated beam is shone on a thin-film sample on a flat substrate and the intensity of the specularly reflected
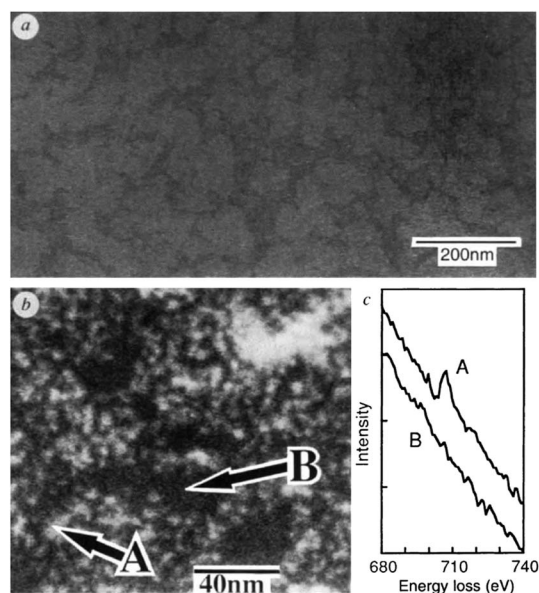

Fig. 5 (a) Bright-field transmission electron micrograph demonstrating the presence of a phase-segregated, interpenetrating network of FeCl₃-stained MEH-PPV (dark regions) and CN-PPV (light regions). In the annular dark-field STEM image (b) the light regions are associated with MEH-PPV, verified by the characteristic iron L-edge peak in the energy-loss spectrum, (c) measured at position A. The dark regions do not contain iron, as shown by the spectrum from position B. Reprinted by permission from Macmillan Publishers Ltd: Nature[17] copyright (1995).
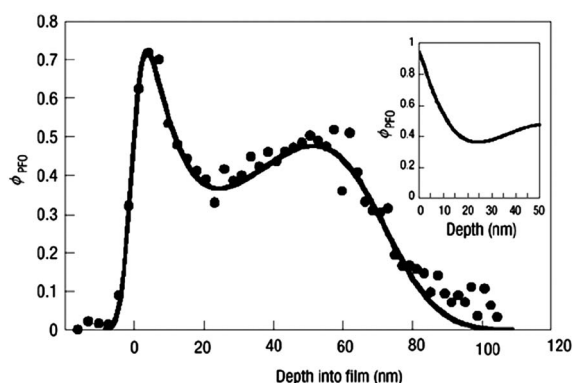
Fig. 6 The d-PFO (deuterated polyfluorene) volume fraction (φ_{PFO}) depth profile of a 70-nm-thick film of a 1 : 1 d-PFO/F8BT blend as determined by nuclear-reaction analysis (see Fig. 7 for chemical structures of PFO and F8BT). The data points (filled circles) show the measured distribution of d-PFO as a function of depth from the film surface. The solid line is a best fit to the data. The inset shows the relative fraction of d-PFO in the near-surface region, extracted from the best-fit analysis (that is, excluding the effect of the finite experimental resolution). It can be seen that at the film surface, the d-PFO fraction approaches unity. Reprinted by permission from Macmillan Publishers Ltd: Nature Materials,[60] copyright (2003).

radiation is measured as a function of angle of incidence. For samples with well-defined layers the reflectivity profile shows Kiessig fringes (see Fig. 14 below) whose spacing is related to the layer thickness, with the attenuation of these fringes providing information about interface roughness. Both neutron[63] and soft X-ray[59,64] beams are able to provide material-specific contrast enabling the interface width of buried interfaces to be determined. Reflectivity techniques can also be used to provide information about surface segregation in blends.[65]

There are many other useful techniques that cannot be covered in detail here, including Raman spectroscopy,[66] near-field scanning optical microscopy,[60,67] and functional scanning probe techniques,[68,69] and the reader is directed to a more comprehensive review of this topic.[70]

5. Domain structure and hierarchical phase separation

It has only been recently that concrete information regarding the sub-100 nm domain structure of all-polymer solar cells has been acquired. Earlier work has either focused on laterally phase-separated blends with mesoscale (100 nm – a few mm) domains[44,71] (whose coarse domain structure is readily imaged by AFM) or relied on photoluminescence quenching measurements to infer information regarding polymer intermixing.[28,47,72] Studies of polymer blends with mesoscale structure has enabled film morphology and device performance to be related,[44,73,74] however it has become clear that there is intermixing within these mesoscale domains[75] and it is the nature of this finer scale intermixing that determines device performance.[73,74]

The morphology of blends of the two polyfluorene co-polymers PFB and F8BT (see Fig. 7 for chemical structures) has been studied in more detail than any other all-polymer system.[15,27,39,44,47,71,74–77] The attention received by this system is
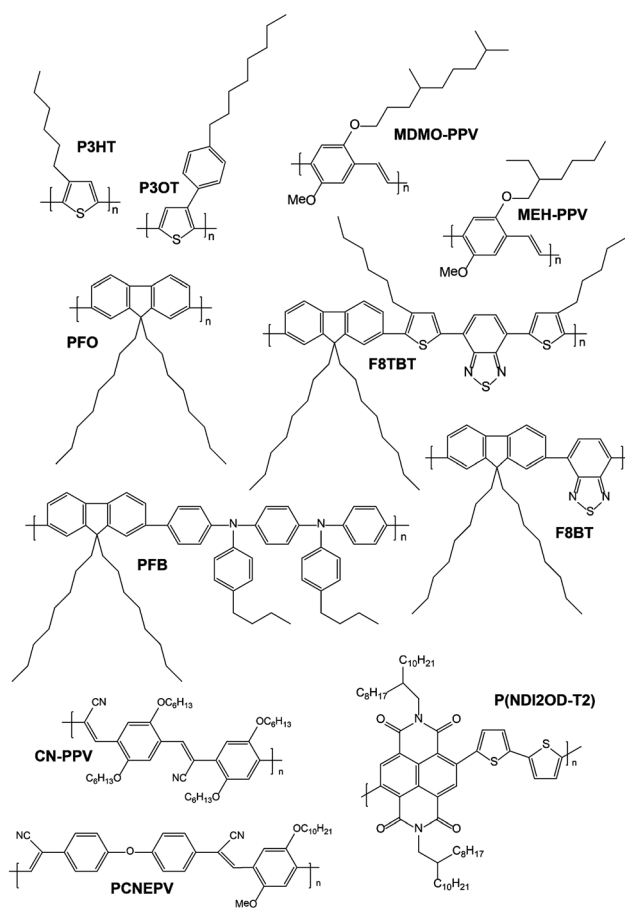

Fig. 7 Chemical structures of polymers discussed in this review.

somewhat surprising given the low efficiencies achieved by PFB: F8BT blends (typically 0.2% or less) however there are a number of factors that make it attractive as a test-bed for examining morphology-performance relationships. Firstly, PFB and F8BT have well-separated absorption and photoluminescence bands, enabling the use of spectroscopic techniques. The high photoluminescence quantum efficiency of the two polymers make the PFB:F8BT system particularly suitable for photoluminescence studies.[27] Secondly, blends prepared from xylene produce laterally phase-separated domains enabling study with scanning probe[44,74] and confocal microscopy.[78] Differences in the NEXAFS spectra of PFB and F8BT also afford good contrast in soft X-ray based experiments.[75] Given that PFB:F8BT blends have received the most comprehensive structural investigation of all polymer/polymer systems, some space will be dedicated here summarising what has been learnt from these studies. This summary will focus on the nanostructured morphology of blends spin-coated from chloroform rather than xylene-processed domains that exhibit lateral, mesoscale domains.

Since chloroform is a good solvent for both PFB and F8BT and given the high volatility of this solvent, the spin-coating of PFB:F8BT blends from chloroform can be expected to produce well-mixed blends. The high photoluminescence quenching (~98%)[27] and smooth surface topography revealed by AFM[38] appear to confirm the intimate mixing of chloroform-processed PFB:F8BT blends. Annealing of chloroform-processed PFB: F8BT blends leads to a coarsening of morphology evidenced by

a systematic increase in photoluminescence yield with annealing temperature. Device performance is found to be optimised for an annealing temperature of ~140 °C. Annealing to 140 °C also produces an increase in photoluminescence yield indicating a trade-off between the dissociation of excitons and the separation/collection of charges, consistent with device simulations.[30,31]

STXM investigations of chloroform-processed PFB:F8BT blends, Fig. 8, reveal domain structure in unannealed films with a characteristic domain size of ~80 nm. This observation is surprising given the high photoluminescence quenching of the as-cast blends and the lack of structure on this lengthscale in AFM images. The efficient photoluminescence quenching however indicates that these 80 nm domains are not pure. Annealing to 140 °C does not lead to any discernable change in domain structure as observed by STXM, Fig. 8, with morphology only seen to evolve with annealing at temperatures above 160 °C. The increase in photoluminescence yield with annealing at temperatures up to 140 °C, Fig. 8f, however, provides evidence for morphological evolution within the 80 nm domains that could not be resolved by STXM (due both to the resolution of the instrument and the fact that STXM is imaging a two-dimensional projection of the three-dimensional morphology). Information regarding the sub-80 nm domain structure and its evolution with annealing has been revealed with R-SoXS measurements. These measurements were performed at a photon energy of 284.7 eV that maximises the scattering contrast between PFB and F8BT and enables structures as small as 4 nm to be probed. Fig. 9 presents the raw scattering profiles and the corresponding pair distribution function. The pair distribution function, $P(r)$, assists interpretation of the scattering data providing ensemble-averaged information about the distances between the phases in the sample and the shape of the domains. The first zero crossing is an indication of the mean domain size, while the magnitude of $P(r)$ is a measure of domain purity. For the as-cast sample the first crossing of $P(r)$ is at ~80 nm matching the domain sizes imaged with X-ray microscopy. With annealing, the magnitude of $P(r)$ systematically increases, however the zero crossing shifts to larger values only for annealing above 160 °C. Thus the morphology evolves initially through a purifying of the 80 nm domains before an evolution in their size.

The R-SoXS data of chloroform-processed blends reveal that a hierarchy of phase separation exists on the sub-100 nm length scale. Hierarchical structures have been observed in other all-polymer systems indicating that they may be a common feature.
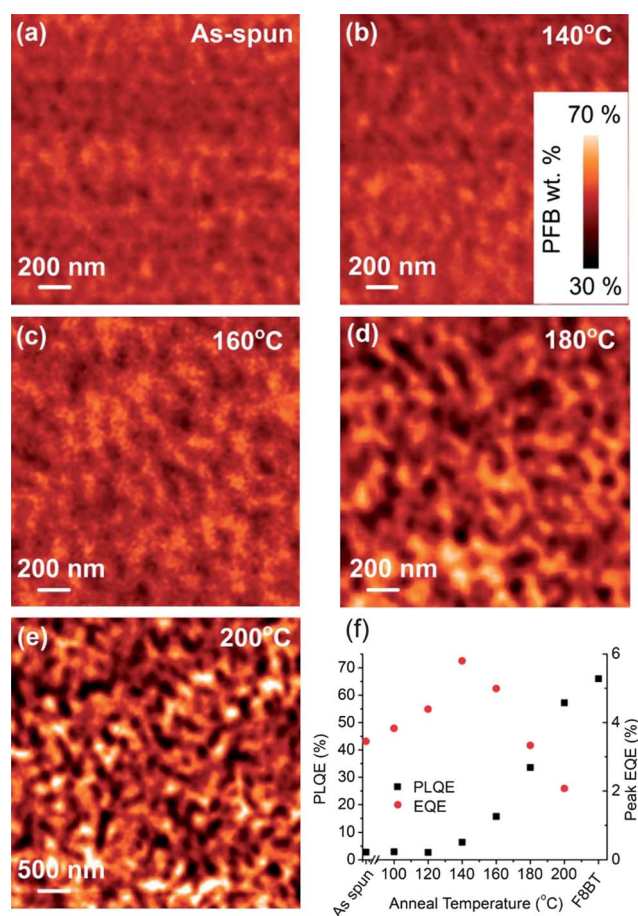

Fig. 8 (a–e) Evolution of the nanomorphology of chloroform-processed PFB:F8BT blends with annealing as imaged by STXM. (f) Evolution of the photoluminescence quantum efficiency (PLQE) and device peak external quantum efficiency (EQE) with annealing. Reproduced with permission from ref. 76. Copyright 2008 Institute of Physics Publishing Ltd.
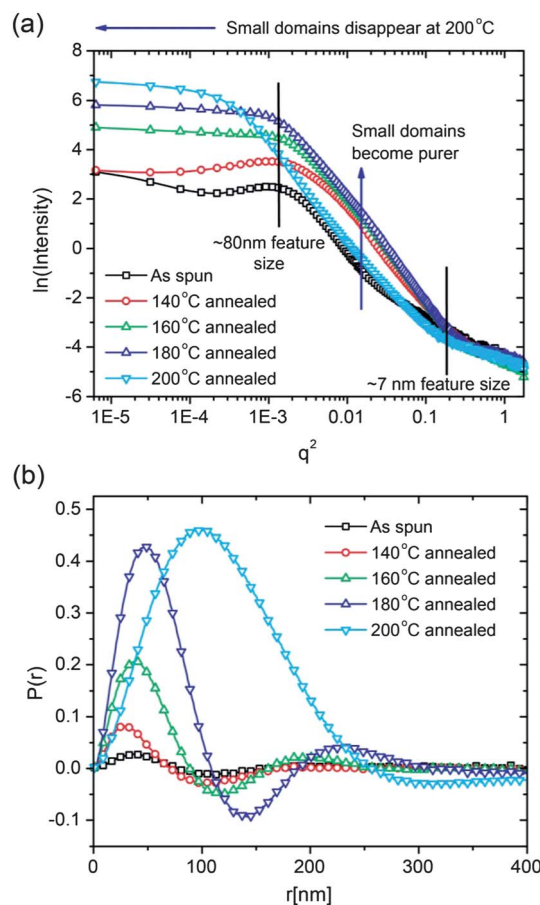

Fig. 9 Resonant soft X-ray scattering profiles of PFB:F8BT blends, (a), and the corresponding pair distribution function, (b). Reprinted (adapted) with permission from ref. 15. Copyright 2010 American Chemical Society.

5660 | *Energy Environ. Sci.*, 2012, **5**, 5653–5667

This journal is © The Royal Society of Chemistry 2012

Loos and co-workers have used zero-loss energy-filtered TEM to investigate the structure of MDMO-PPV:PCNEPV blends with different molecular weight, see Fig. 10. Structure is seen in these images, with the films with higher molecular weight exhibiting larger-sized structures. Nitrogen elemental maps confirm that the features seen in Fig. 10 are the result of chemical contrast rather than thickness variations with the dark regions corresponding to PCNEPV-rich domains.[79] These MDMO-PPV:PCNEPV films

were prepared with a weight ratio of 1 : 1, however examining the images of Fig. 10 it is clear that the PCNEPV domains do not fill 50% of the images, providing a clear indication of intermixing with phases, confirmed by fluorescence quenching measurements. Strikingly, the device performance of blends based on such films are very similar, suggesting that device performance is more sensitive to the finer-scale intermixing than the large features observed in these TEM images. Fig. 11 presents STXM images of the P3HT:P(NDI2OD-T2) system for 1 : 1 blends prepared from different solvents before and after annealing. Domains are readily observed with STXM for all casting solvents. STXM detects little change in with annealing, despite annealing being required to optimise device performance. Chloroform-processed blends were found to have the best efficiency and exhibit the finest domain structure, with characteristic domain size of ~200 nm as seen by STXM. Much coarser domain structure is observed in the dichlorobenzene- and xylene-processed blends, with domains on the length-scale of 500 nm to 1 mm. Interestingly devices based on the xylene-processed blends that have the largest structure were found to have higher efficiency than dichlorobenzene-processed blends suggesting that again it is the intermixing within these coarser domains that is determining cell efficiency. Indeed, results from a R-SoXS investigation has confirmed the presence of domains on the 5–20 nm length scale that evolve with annealing, with a concomitant evolution of device performance.[80]

Under the conventional bulk heterojunction model, blends with structure much larger than the exciton diffusion length are expected to be inferior to the 'ideal' morphology consisting of pure domains structured on the 10–20 nm length-scale. While
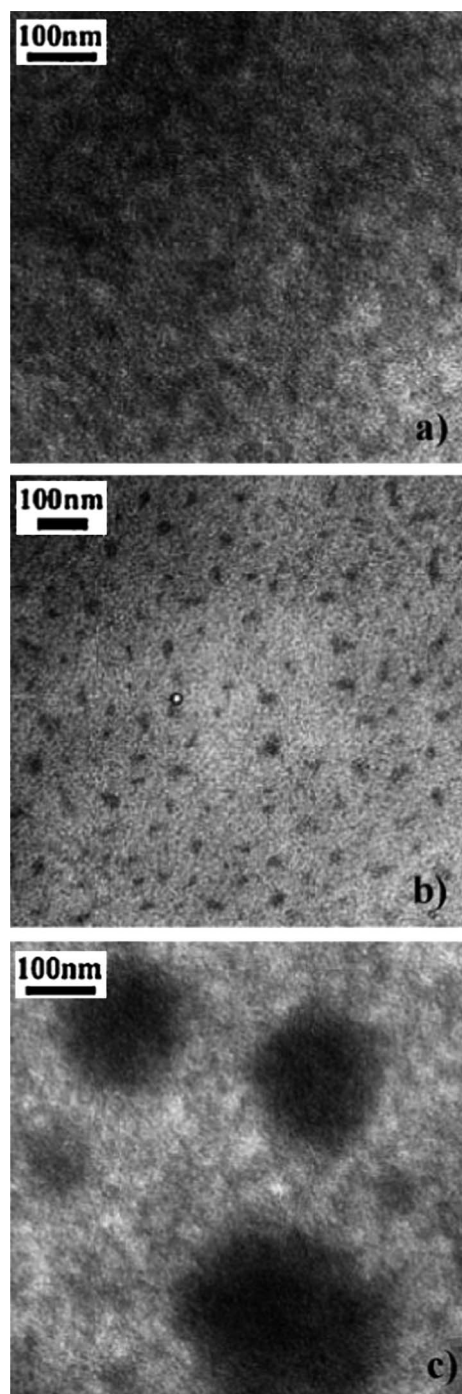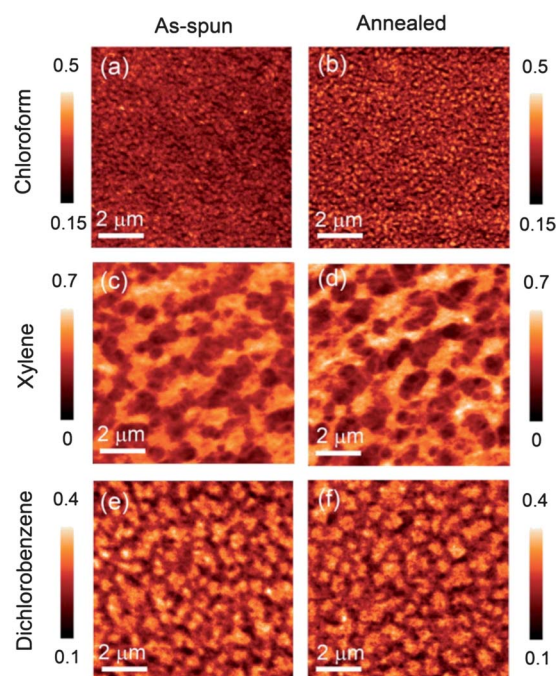

Fig. 10 Zero-loss energy-filtered transmission electron microscopy images of MDMO-PPV:PCNEPV blends with low, (a), medium, (b) and high, (c), molecular weights of PCNEPV. Reprinted with permission from ref. 43. Copyright 2007 Wiley-VCH.

Fig. 11 STXM optical density images of as-spun (a,c,e) and annealed (b, d,f) P3HT:P(NDI2OD-T2) films spin-coated from either chloroform (a, b) xylene (c,d) or dichlorobenzene (e,f). Images were acquired at a photon energy of 285 eV corresponding to preferential absorption by P3HT. Reprinted with permission from ref. 81. Copyright 2011 Wiley-VCH.

these coarser domains are intermixed, the inability to control the local blend ratio *via* solution-processing potentially hinders device optimisation. Hierarchical domains have also been observed in polymer/fullerene blends where it has been proposed that such morphologies may actually be beneficial for device operation challenging our assumptions about what constitutes an 'ideal morphology'.[56,82] Nevertheless, the observation of hierarchical domain structures indicates that our ability to control the domain structure of bulk heterojunction blends on the sub-100 nm length scale *via* solution processing methods leaves much to be desired.

6. Interface structure

There are many interfaces in a polymer blend device that are important for device operation. Within the blend itself there are the interfaces between donor and acceptor domains, while at the blend/electrode interfaces the surface composition can also influence charge extraction. Considering the blend/electrode interfaces first, the different surface energies of the two polymers generally results in the enrichment of one polymer at one or both blend/electrode interfaces.[35,36,46,60] Having the 'wrong' material at one of the blend/electrode interfaces (*e.g.* a wetting layer of the electron donating polymer at the interface with the electron collecting contact) may result in inferior device performance. For blends of P3HT with F8TBT wetting layers of P3HT have been observed with XPS at both blend/electrode interfaces in as-spun (unannealed) films, with a surface compositions greater than 0.95 P3HT.[46] Annealing of films in the presence of a top aluminium electrode ('post-anneal') was found to result in an increase in the surface composition of the electron accepting F8TBT from less than 0.05 to ~0.15. In contrast, annealing in the absence of a top aluminium electrode ('pre-anneal') resulted in no observable change in surface composition. A large difference in the device performance of pre- and post-annealed devices was observed, with the post-annealed devices 6 times as efficient as the pre-annealed devices due to superior short-circuit current and open circuit voltage.[46] Lyons *et al.* have used a combination of modelling approaches to examine the quantitative effect of surface wetting layers on the performance of bulk heterojunction devices.[83] Fig. 12a presents example morphologies generated using a modified version of Cahn-Hilliard theory with donor and acceptor phases having equal molecular weight. One blend shown in Fig. 12a has surface effects turned off resulting in a surface composition of 0.5 (equal amounts of donor and acceptor at the interface) while for the other morphology surface effects are included resulting in a complete covering of the surface by one phase (composition of 1). By variation of the simulation conditions, blends with surface compositions ranging from 0 to 1 can be produced allowing comparison of 'favourable,' 'neutral' and 'blocking' surfaces. The influence of surface composition on short-circuit current is presented in Fig. 12b. Surprisingly both 'favourable' and 'blocking' surfaces are found to hamper charge extraction relative to a neutral surface layer, with performance dropping sharply for surface compositions of either material above 0.85.[83] The reason why 'favourable' as well as 'blocking' surfaces are detrimental to charge extraction is due to the presence of a subsurface layer that mirrors the surface layer as seen in Fig. 12a. Thus if the surface is completely covered
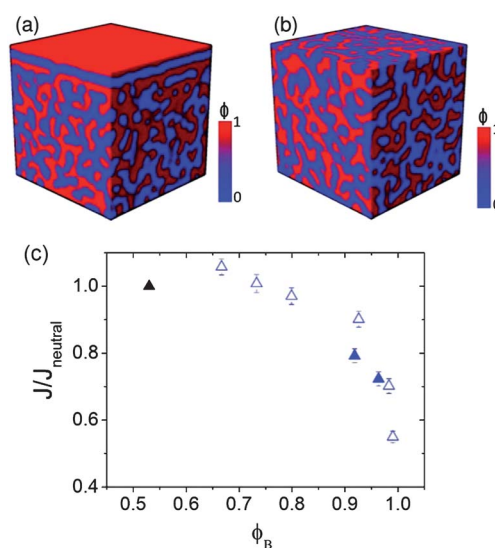

Fig. 12 Examples of morphologies generated using a modified version of Cahn-Hilliard theory with donor and acceptor phases having equal molecular weight. The morphology in part (a) exhibits a closed wetting layer, while the morphology in part (b) has surface effects turned off. (c) Effect of surface composition on photocurrent relative to a 'neutral' surface with surface composition of 0.5. Black, open blue, and filled blue symbols correspond to morphologies with 'neutral,' 'favourable' and 'blocking' surfaces, respectively. Reprinted (adapted) with permission from ref. 83. Copyright 2011 American Chemical Society.

by 'correct' material, it is likely that there is a subsurface layer of the 'wrong' material that is as effective as a surface wetting layer at blocking charge extraction.

Although little is known about the nature of donor/acceptor interfaces in bulk heterojunction blends, interfacial processes such as exciton dissociation and interfacial charge separation are critical steps in device operation. The nature of donor/acceptor interfaces concerns both the conformational nature of donor and acceptor materials on the molecular level, as well the interfacial width of domain boundaries. Quantum chemical calculations have shown that different geometric configurations of donor and acceptor chains at a heterojunction lead to interfacial excited states with differing electronic character.[84] Holcombe *et al.* have compared the operation of all-polymer solar cells using P3HT and POPT as the electron donor, see Fig. 13.[85] The bulky side group on POPT chains leads to increased physical separation of donor/acceptor chains at the heterojunction, leading to a decrease in the energy of relaxed interfacial electron-hole pairs, reducing the barrier to charge separation. Studying blends with a number of polymer acceptors, the performance of POPT-based cells was found to be consistently higher than that of P3HT-based devices providing strong evidence for a connection between device performance and heterojunction conformation.[85]

While it is extremely difficult to experimentally characterize the precise molecular conformation of donor and acceptor chains at heterojunctions within a polymer blend, experimental insight into the influence of interface structure on device performance can be gained through the study of bilayer structures. Although bilayer devices are less efficient than blends, the planar structure allows for the interface width to be measured with reflectivity techniques.[63,86] Fig. 14a presents resonant soft X-ray reflectivity
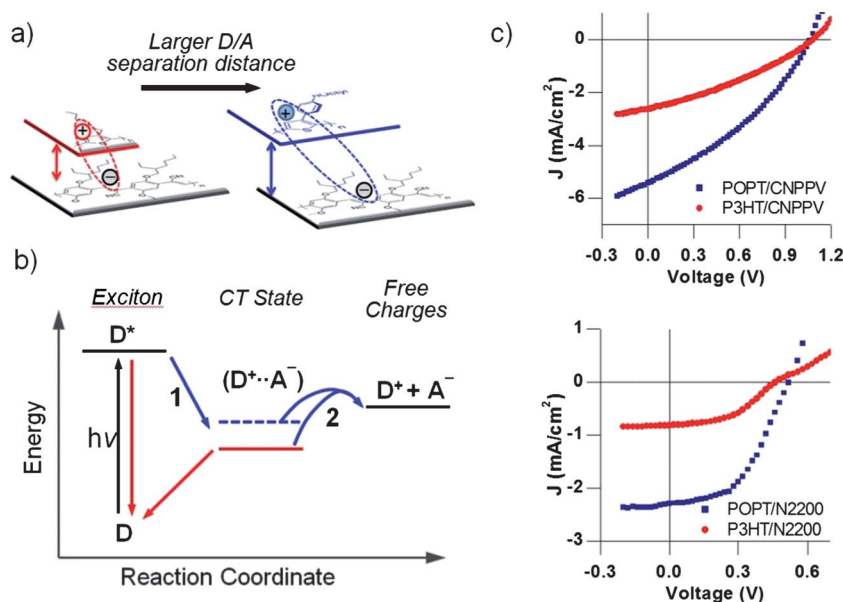
Fig. 13 (a, b) Schematic diagrams demonstrating how steric interactions can lead to an increase in backbone spacing and destabilization of the geminate pair due to a different energy landscape. (c) Example current voltage curves showing the enhanced performance of POPT-based devices compared to P3HT-based devices. 'N2200' is the polymer P(NDI2OD-T2). Reprinted (adapted) with permission from ref. 10. Copyright 2011 American Chemical Society.

data of laminated PFB/F8BT bilayers that have been annealed at different temperatures.[86] The soft X-ray energy used has been chosen to maximize sensitivity to the buried PFB/F8BT interface. The reflectance profile of the unannealed bilayer shows well-defined fringe modulations with an interface width of 0.68 nm as determined by the numerical fit. With annealing the fringes become less prominent due to broadening of the PFB/F8BT interface, with the fitted interface width systematically increasing from 0.68 nm to 6.7 nm, see Fig. 14b. Although an increased interface width should be beneficial to device performance due to increased exciton dissociation yield, surprisingly device performance was found to decrease with annealing. Device simulations, incorporating changes in interface width and charge carrier mobility with annealing, were able to confirm this trend indicating that while a roughened interface may be beneficial for charge generation (exciton dissociation) it can be detrimental to charge separation hindering the separation of interfacial electron-hole pairs.[86] Since non-equilibrium sharp interfaces that favour charge separation are not produce by phase separation within a blend (the interface width sharpens as phase separation evolves and generally converges to a non-zero value[33]) the interface width in solution-processed blends may always be in some way non-optimal. It should be noted that the nature of interfaces and material interdiffusion are also important for polymer/fullerene cells. However recent research has shown the ability for fullerene molecules to rapidly interdiffuse into neat polymer films observed *via* the preparation of polymer/fullerene bilayers[87,88] making artificial, sharp interfaces less stable to thermal treatment.

7. Novel routes for morphological control

As highlighted in the previous sections, the use of solution processing and annealing in general only allows for rudimentary

morphological control. In this last section, novel approaches for controlling morphology that provide a greater degree of morphological control, including nano-imprint lithography and block copolymers are presented.

A key goal of morphological control is the ability to precisely control domain size. The miniemulsion process is a convenient solution-processing technique that enables the creation of polymer nanoparticles of well-defined size, see Fig. 15.[89,90] A solution of polymer is first prepared in an organic solvent that is then mixed with water containing an appropriate surfactant. Stirring and ultrasonication leads to the formation of a miniemulsion with drops of the polymer solution stabilised in the aqueous solution by the surfactant. The polymer solvent is then evaporated leaving an aqueous dispersion of solid polymer nanoparticles from which a film of nanoparticles can be deposited. Nanoparticles of donor and acceptor polymers can be prepared separately and the two different dispersions blended to produce a mixed film of donor and acceptor nanoparticles. Alternatively, a polymer blend solution can be used to form an emulsion of blended polymer nanoparticles. In both cases the upper limit for the dimension of phase separation is determined by the size of the individual nanoparticles. A limitation of this approach is that the smallest size nanoparticles that can be produced is a few tens of nanometres[90] that is larger than the exciton diffusion length. Furthermore, the morphology of blended nanospheres may adopt a core-shell structure that may not be ideal for device operation,[91] and the formation of percolation pathways is not guaranteed.

Another approach that affords versatility in the range of solution-processed structures that can be produced is through the use of a sacrificial, insulating polymer that acts a phase-directing agent (PDA), see Fig. 16.[77] This phase-directing polymer is blended with one of the conjugated polymers to be used, typically the donor polymer. In addition to being soluble in a common solvent with the donor polymer, the PDA is chosen
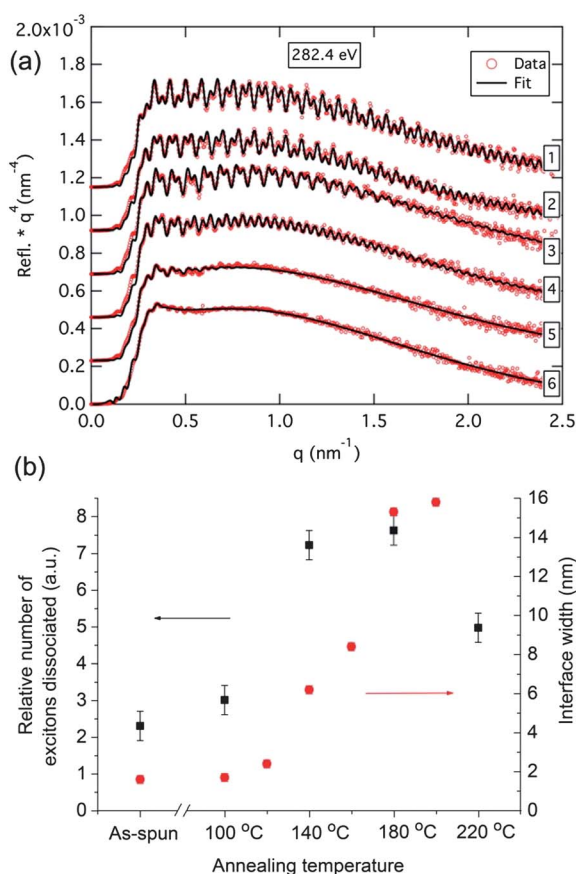
Fig. 14 (a) Resonant soft X-ray reflectivity profiles (data – circles, solid line - fit) of PFB/F8BT bilayers as a function of annealing. (1) as-prepared, (2) 100 °C, (3) 120 °C, (4) 140 °C, (5) 160 °C, and (6) 200 °C. The loss of the fringe modulations at higher annealing temperatures directly indicates an increase in polymer/polymer interfacial width. (b) Evolution of interface width (determined from the numerical fits) and exciton quenching efficiency with annealing. Reprinted (amended) with permission from ref. 86. Copyright 2007 Wiley-VCH.

such that it is soluble in a solvent that the donor polymer is not soluble in. Once a blend of the donor polymer and PDA is cast, the PDA can be washed away leaving a porous nanostructured matrix. The donor matrix is then cross-linked and back-filled with the acceptor phase. The use of a PDA offers greater flexibility in tuning of morphology as the physical properties of the PDA (polymer type, molecular weight) can be changed without the need to change the acceptor polymer. This approach also avoids intermixing of donor and acceptor phases, though a minority component of the PDA is likely to remain in the donor phase. Superior device efficiencies have been demonstrated for PFB/F8BT structures prepared in this way compared to conventional blends,[77] however demonstration of efficiencies beyond state-of-the-art are yet to be realised. There are also potential issues associated with attaining phase-separated structures on the length scale of 10–20 nm due to the potential difficulty of washing away and backfilling into nanoporous structures on such a length scale (50 nm is the smallest lateral feature demonstrated to date[77]).

Nanoimprint lithography utilises the predefined nanostructures of an electron-beam patterned master to create
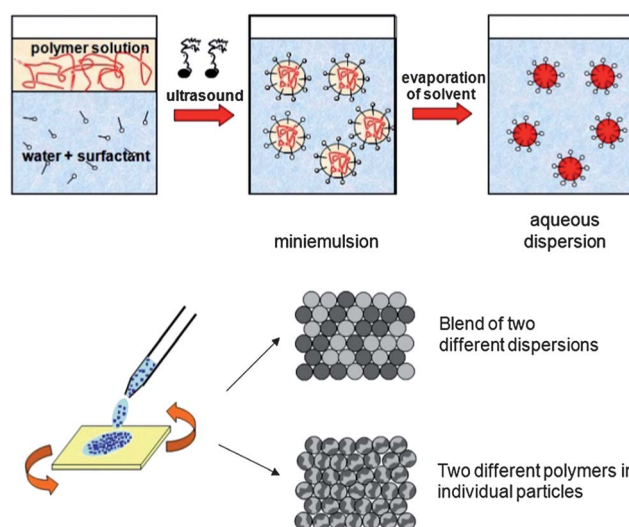

Fig. 15 Schematic of the process of preparing polymer nanoparticles and films *via* a miniemulsion route. (a) First, a solution of the polymer in an organic solvent is mixed with water containing an appropriate surfactant. A miniemulsion is then formed on stirring and ultrasonication. Finally, the solvent is evaporated, resulting in solid polymer nanoparticles dispersed in water. (b) Phase-separated structures at the nanometre scale can be prepared either by coating a layer from a dispersion containing nanoparticles of two different polymers, or by using dispersions that contain both polymers in each individual nanoparticle. Reprinted by permission from Macmillan Publishers Ltd: Nature Materials,[90] copyright (2003).

nanostructured donor/acceptor interfaces, see Fig. 17. The dual imprint technique developed by He *et al.*[92] uses a nanoimprinted film of one of the donor/acceptor polymer pair as a master to imprint into the other polymer forming a nanostructured, interpenetrating heterojunction device. These structures ensure complete coverage of the anode by the electron donating polymer and of the cathode by the electron accepting polymer. P3HT/F8BT nanoimprinted devices have been fabricated with a power conversion efficiency twice that of a control blend device (using a 25 nm diameter columns with 50 nm pitch),[92] and equal to the best previously reported efficiency reported for P3HT/F8BT blends. A strong correlation between the feature size of the nanoimprinted structure and device performance was also observed, consistent with the increased interfacial area. Structures finer than 25 nm were not able to be produced, however, due to the instability of high aspect ratio imprinted structures. Nevertheless, these results are very encouraging and demonstrate that improved control of film morphology is indeed a promising route to engineering efficiency improvements.

Block co-polymers are an exciting class of material that has the potential to provide exquisite control of nanomorphology through chemical synthesis. Block copolymers for organic photovoltaics is a significant topic in itself has been covered by a number of recent review articles,[93–96] with the discussion here providing only a brief overview of the subject. The covalent linking of two different polymer 'blocks' prevents phase separation of the two chemically distinct chain segments. Under certain conditions, namely for $\chi N \gg 10$ where χ is the Flory-Huggins interaction parameter and N is the chain length of the block copolymer, energetic factors dominate over entropic

5664 | *Energy Environ. Sci.*, 2012, **5**, 5653–5667

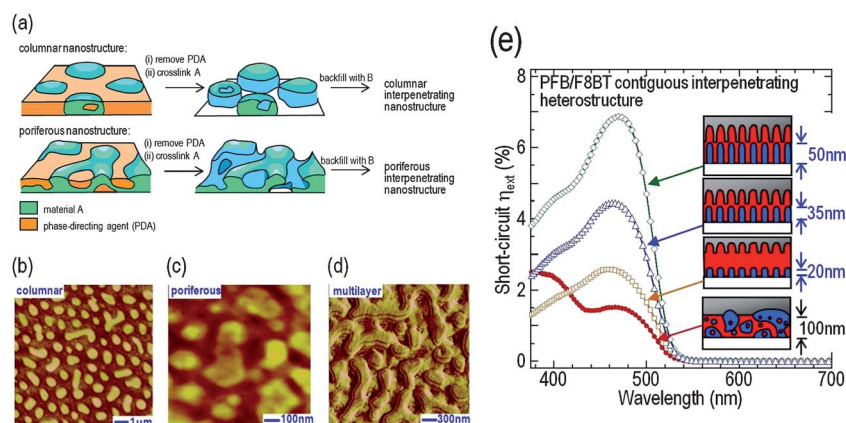This journal is © The Royal Society of Chemistry 2012

Fig. 16 a) Schematic of the process for forming nanostructured donor/acceptor blends through the use of a sacrificial phase-directing agent (PDA). The donor polymer is mixed with the PDA to form a phase-separated blend structure. The PDA is then dissolved, the donor polymer cross-linked and the structure back-filled with the acceptor polymer. (a–d) AFM images of morphologies produced. (e) Comparison of the performance of PFB:F8BT devices fabricated through conventional blending and through the use of a PDA. Adapted and reprinted by permission from Macmillan Publishers Ltd: Nature Materials,[77] copyright (2009).

considerations resulting in the formation of ordered nano-structures characterised by narrow interfaces and nearly flat composition profiles.[97] Furthermore, by changing the volume fraction f of the blocks, where $f = \frac{1}{2}$ corresponds to the symmetric case, a range of ordered phases with different symmetries can be produced as illustrated in Fig. 18. The majority of block copolymer research historically has been based on insulating coil-coil block-copolymers. While of great interest for nanolithographic applications such materials are of little direct use for optoelectronic applications. The use of semi-conducting block copolymers presents new challenges due to the nonidealities in molecular conformation and mixing interactions commonly present in conjugated polymers.[93] Conjugation serves to rigidify the backbone to form rod-like chains and introduce liquid crystalline interactions, leading to the formation of rod-coil or rod-rod block copolymers.[96,98] The phase behaviour of
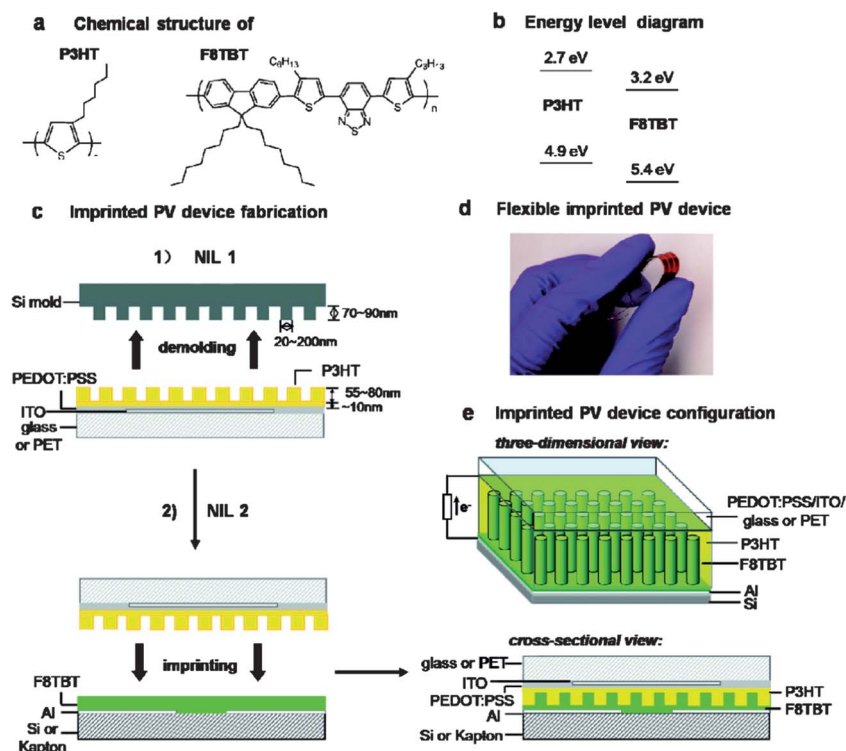

Fig. 17 (a) Chemical structures and (b) energy levels of P3HT and F8TBT. (c) Schematic of the nano-imprinting device fabrication procedure, (1) Patterning of a P3HT film spin-cast on an ITO/glass substrate coated with PEDOT:PSS using a silicon mould. (2) The patterned P3HT film is used as a mould to imprint an F8TBT film spin-cast on an aluminium-coated silicon wafer or Kapton substrate resulting in a double-imprinted device. (d) Photograph of a flexible double-imprinted P3HT/F8TBT device fabricated using PET and Kapton polyimide films. (e) Three-dimensional and cross-sectional view of the imprinted device configuration. Reprinted with permission from ref. 92. Copyright (2010) American Chemical Society.

rod-coil block copolymers, for example, requires two additional parameters in addition to χN resulting in a 4-dimensional phase diagram.[93] Thus control of the phase behaviour of conjugated block copolymers is especially challenging. In addition to their complex phase behaviour, the synthesis of conjugated block copolymers is also difficult, with control of chain length and polydispersity required for block copolymers incorporating rod-like blocks. As a result of these challenges, the demonstration of well-organized nanostructures with fully conjugated blocks has been limited,[99] and device applications scarcer.[100] Some success has been achieved with block copolymers composed of a rod-like P3HT donor block with a coil-like acceptor block consisting of a saturated backbone but with pendant perylene diimide units,[101] encouraging further work in this area. Achieving efficiencies beyond state-of-the-art with semiconducting block copolymers, however, still seems some way away.

8.   Conclusions and outlook

Our understanding of the nanomorphology of all-polymer solar cells has improved dramatically in recent years with device performance correlated with experimentally determined sub-100 nm domain sizes. These morphology studies have shown that hierarchical phase-separated structures are commonly observed demonstrating that only rudimentary control over domain structure is afforded by conventional solution processing and annealing techniques. Studies are now beginning to focus on the influence of donor/acceptor interface structure on device performance, and have highlighted the sensitivity of device performance to interface width and the molecular conformation of donor/acceptor heterojunctions. Numerical simulations have been invaluable in allowing morphology and device performance to be studied in controlled systems, and there is the tantalising prospect that in the near future experimentally determined morphologies may be used as input morphologies in these simulations. A key question for device simulations is whether the hierarchical morphologies typically observed are beneficial or detrimental for device performance. Novel routes for morphological will continue to be important in providing experimentally-controlled morphologies for both device studies and efficiency improvements. These developments in morphological characterisation and control, combined with dedicated synthetic effort in the development of new donor and acceptor polymers,
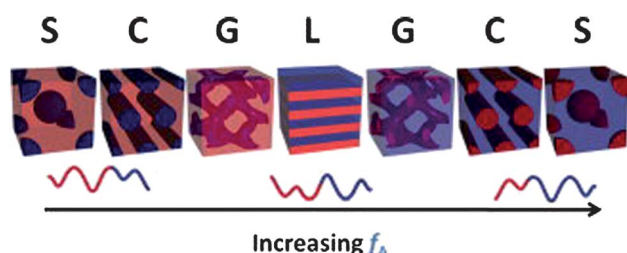
will hopefully lead to significant improvements in device efficiency enabling all-polymer blends to compete with other classes of organic solar cells.

References

1 F. C. Krebs, T. Tromholt and M. Jorgensen, *Nanoscale*, 2010, **2**, 873.
2 S. E. Shaheen, C. J. Brabec, N. S. Sariciftci, F. Padinger, T. Fromherz and J. C. Hummelen, *Appl. Phys. Lett.*, 2001, **78**, 841.
3 Z. He, C. Zhong, X. Huang, W.-Y. Wong, H. Wu, L. Chen, S. Su and Y. Cao, *Adv. Mater.*, 2011, **23**, 4636.
4 C. H. Peters, I. T. Sachs-Quitana, J. P. Kastrop, S. Beaupré, M. Leclerc and M. D. McGehee, *Adv. Energy Mater.*, 2011, **1**, 491.
5 P. W. M. Blom, V. D. Mihailetchi, L. J. A. Koster and D. E. Markov, *Adv. Mater.*, 2007, **19**, 1551.
6 C. J. Brabec, S. Gowrisanker, J. J. M. Halls, D. Laird, S. Jia and S. P. Williams, *Adv. Mater.*, 2010, **22**, 3839.
7 W. U. Huynh, J. J. Dittmer and A. P. Alivisatos, *Science*, 2002, **295**, 2425.
8 C. R. McNeill, *J. Polym. Sci., Part B: Polym. Phys.*, 2011, **49**, 909.
9 S. Dayal, N. Kopidakis, D. C. Olson, D. S. Ginley and G. Rumbles, *Nano Lett.*, 2009, **10**, 239.
10 T. W. Holcombe, J. E. Norton, J. Rivnay, C. H. Woo, L. Goris, C. Piliego, G. Griffini, A. Sellinger, J.-L. Brédas, A. Salleo and J. M. J. Fréchet, *J. Am. Chem. Soc.*, 2011, **133**, 12106.
11 D. Mori, H. Benten, J. Kosaka, H. Ohkita, S. Ito and K. Miyake, *ACS Appl. Mater. Interfaces*, 2011, **3**, 2924.
12 E. Zhou, J. Cong, Q. Wei, K. Tajima, C. Yang and K. Hashimoto, *Angew. Chem., Int. Ed.*, 2011, **50**, 2799.
13 J. M. Hodgkiss, A. R. Campbell, R. A. Marsh, A. Rao, S. Albert-Seifried and R. H. Friend, *Phys. Rev. Lett.*, 2010, **104**, 177701.
14 R. A. Marsh, C. R. McNeill, A. Abrusci, A. R. Campbell and R. H. Friend, *Nano Lett.*, 2008, **8**, 1393.
15 S. Swaraj, C. Wang, H. Yan, B. Watts, J. Lüning, C. R. McNeill and H. Ade, *Nano Lett.*, 2010, **10**, 2863.
16 D. E. Markov, E. Amsterdam, P. W. M. Blom, A. B. Sieval and J. C. Hummelen, *J. Phys. Chem. A*, 2005, **109**, 5266.
17 J. J. M. Halls, C. A. Walsh, N. C. Greenham, E. A. Marseglia, R. H. Friend, S. C. Moratti and A. B. Holmes, *Nature*, 1995, **376**, 498.
18 G. Yu, J. Gao, J. C. Hummelen, F. Wudl and A. J. Heeger, *Science*, 1995, **270**, 1789.
19 G. Yu and A. J. Heeger, *J. Appl. Phys.*, 1995, **78**, 4510.
20 F. C. Jamieson, T. Agostinelli, H. Azimi, J. Nelson and J. R. Durrant, *J. Phys. Chem. Lett.*, 2010, **1**, 3306.
21 R. A. Marsh, J. M. Hodgkiss and R. H. Friend, *Adv. Mater.*, 2010, **22**, 3672.
22 J. H. Lee, K. Vandewal, S. R. Yost, M. E. Bahlke, L. Goris, M. A. Baldo, J. V. Manca and T. V. Voorhis, *J. Am. Chem. Soc.*, 2010, **132**, 11878.
23 H. Ohkita, S. Cook, Y. Astuti, W. Duffy, S. Tierney, W. Zhang, M. Heeney, L. McCulloch, J. Nelson, D. D. C. Bradley and J. R. Durrant, *J. Am. Chem. Soc.*, 2008, **130**, 3030.
24 H. Aarnio, P. Sehati, S. Braun, M. Nyman, M. P. de Jong, M. Fahlman and R. Österbacka, *Adv. Energy Mater.*, 2011, **1**, 792.
25 R. I. Gearba, T. Mills, J. Morris, R. Pindak, C. T. Black and X. Zhu, *Adv. Funct. Mater.*, 2011, **21**, 2666.
26 M. M. Mandoc, W. Veurman, L. J. A. Koster, B. de Boer and P. W. M. Blom, *Adv. Funct. Mater.*, 2007, **17**, 2167.
27 C. R. McNeill, S. Westenhoff, C. Groves, R. H. Friend and N. C. Greenham, *J. Phys. Chem. C*, 2007, **111**, 19153.
28 C. Yin, T. Kietzke, D. Neher and H. H. Hörhold, *Appl. Phys. Lett.*, 2007, **90**, 092117.
29 A. Pivrikas, G. Juška, A. J. Mozer, M. Scharber, K. Arlauskas, N. S. Sariciftci, H. Stubb and R. Österbacka, *Phys. Rev. Lett.*, 2005, **94**, 176806.
30 P. K. Watkins, A. B. Walker and G. L. B. Verschoor, *Nano Lett.*, 2005, **5**, 1814.
31 C. Groves, R. A. Marsh and N. C. Greenham, *J. Chem. Phys.*, 2008, **129**, 114903.
32 D. Veldman, O. Ipek, S. C. J. Meskers, J. Sweelssen, M. M. Koetse, S. C. Veenstra, J. M. Kroon, S. S. van Bavel, J. Loos and R. A. J. Janssen, *J. Am. Chem. Soc.*, 2008, **130**, 7721.

Fig. 18 Schematics of the most commonly observed nanostructures adopted by coil-coil block copolymers, where S = spheres, C = cylinders, G = gyroid and L = lamellae. The blue block indicates polymer A (with volume fraction, f_A) and the red block polymer B. Reprinted with permission from ref. 95. Note that many of the structures pictured here may be hard to obtain with fully conjugated polymers since they are stiffer than coil-type polymers. Copyright 2007 Wiley-VCH.

33 R. A. L. Jones and R. W. Richards, *Polymers at Surfaces and Interfaces*, Cambridge University Press, Cambridge, 1999.
34 A. C. Arias, N. Corcoran, M. Banach, R. H. Friend, J. D. MacKenzie and W. T. S. Huck, *Appl. Phys. Lett.*, 2002, **80**, 1695.
35 A. M. Higgins, S. J. Martin, R. J. Thompson, J. Chappell, M. Voigt, D. G. Lidzey, R. A. L. Jones and M. Geoghegan, *J. Phys.: Condens. Matter*, 2005, **17**, 1319.
36 J. S. Kim, P. K. H. Ho, C. E. Murphy and R. H. Friend, *Macromolecules*, 2004, **37**, 2861.
37 S. Y. Heriot and R. A. L. Jones, *Nat. Mater.*, 2005, **4**, 782.
38 A. C. Arias, J. D. MacKenzie, R. Stevenson, J. J. M. Halls, M. Inbasekaran, E. P. Woo, D. Richards and R. H. Friend, *Macromolecules*, 2001, **34**, 6005.
39 H. J. Snaith and R. H. Friend, *Thin Solid Films*, 2004, **451–452**, 567.
40 A. R. Campbell, J. M. Hodgkiss, S. Westenhoff, I. A. Howard, R. A. Marsh, C. R. McNeill, R. H. Friend and N. C. Greenham, *Nano Lett.*, 2008, **8**, 3942.
41 G. Li, V. Shrotriya, J. Huang, Y. Yao, T. Moriarty, K. Emery and Y. Yang, *Nat. Mater.*, 2005, **4**, 864.
42 J. Peet, M. L. Senatore, A. J. Heeger and G. C. Bazan, *Adv. Mater.*, 2009, **21**, 1521.
43 S. C. Veenstra, J. Loos and J. M. Kroon, *Progr. Photovolt.: Res. Appl.*, 2007, **15**, 727.
44 H. J. Snaith, A. C. Arias, A. C. Morteani, C. Silva and R. H. Friend, *Nano Lett.*, 2002, **2**, 1353.
45 S. Fabiano, Z. Chen, S. Vahedi, A. Facchetti, B. Pignataro and M. A. Loi, *J. Mater. Chem.*, 2011, **21**, 5891.
46 C. R. McNeill, J. J. M. Halls, R. Wilson, G. L. Whiting, S. Berkebile, M. G. Ramsey, R. H. Friend and N. C. Greenham, *Adv. Funct. Mater.*, 2008, **18**, 2309.
47 S. Westenhoff, I. A. Howard and R. H. Friend, *Phys. Rev. Lett.*, 2008, **101**, 016102.
48 X. Yang, J. Loos, S. C. Veenstra, W. J. H. Verhees, M. M. Wienk, J. M. Kroon, M. A. J. Michels and R. A. J. Janssen, *Nano Lett.*, 2005, **5**, 579.
49 J. Loos, X. Yang, M. M. Koetse, J. Sweelssen, H. F. M. Schoo, S. C. Veenstra, W. Grogger, G. Kothleitner and F. Hofer, *J. Appl. Polym. Sci.*, 2005, **97**, 1001.
50 D. R. Kozub, K. Vakhshouri, L. M. Orme, C. Wang, A. Hexemer and E. D. Gomez, *Macromolecules*, 2011, **44**, 5722.
51 H. Ade, X. Zhang, S. Cameron, C. Costello, J. Kirz and S. Williams, *Science*, 1992, **258**, 972.
52 H. Ade and H. Stoll, *Nat. Mater.*, 2009, **8**, 281.
53 S. S. van Bavel, S. Sourty, G. de With and J. Loos, *Nano Lett.*, 2009, **9**, 507.
54 G. A. Johansson, T. Tyliszczak, G. E. Mitchell, M. H. Keefe and A. P. Hitchcock, *J. Synchrotron Radiat.*, 2007, **14**, 395.
55 J. W. Kiel, A. P. R. Eberle and M. E. Mackay, *Phys. Rev. Lett.*, 2010, **105**, 168701.
56 W. Yin and M. Dadmun, *ACS Nano*, 2011, **5**, 4756.
57 A. J. Parnell, A. J. Cadby, O. O. Mykhaylyk, A. D. F. Dunbar, P. E. Hopkinson, A. M. Donald and R. A. L. Jones, *Macromolecules*, 2011, **44**, 6503.
58 C. Wang, T. Araki, B. Watts, S. Harton, T. Koga, S. Basu and H. Ade, *J. Vac. Sci. Technol., A*, 2007, **25**, 575.
59 S. Swaraj, C. Wang, T. Araki, G. E. Mitchell, L. Liu, S. Gaynor, B. Deshmukh, Y. Yan, C. R. McNeill and H. Ade, *Eur. Phys. J. Spec.Top.*, 2009, **168**, 121.
60 J. Chappell, D. G. Lidzey, P. C. Jukes, A. M. Higgins, R. L. Thompson, S. O'Connor, I. Grizzi, R. Fletcher, J. O'Brien, M. Geoghegan and R. A. L. Jones, *Nat. Mater.*, 2003, **2**, 616.
61 Y. Vaynzof, D. Kabra, L. Zhao, L. L. Chua, U. Steiner and R. H. Friend, *ACS Nano*, 2010, **5**, 329.
62 C. M. Björström, *et al.*, *J. Phys.: Condens. Matter*, 2005, **17**, L529.
63 A. M. Higgins, A. Cadby, D. G. Lidzey, R. M. Dalgliesh, M. Geoghegan, R. A. L. Jones, S. J. Martin and S. Y. Heriot, *Adv. Funct. Mater.*, 2009, **19**, 157.
64 C. Wang, T. Araki and H. Ade, *Appl. Phys. Lett.*, 2005, **87**, 214109.
65 A. J. Parnell, A. D. F. Dunbar, A. J. Pearson, P. A. Staniec, A. J. C. Dennison, H. Hamamatsu, M. W. A. Skoda, D. G. Lidzey and R. A. L. Jones, *Adv. Mater.*, 2010, **22**, 2444.
66 R. Stevenson, A. C. Arias, C. Ramsdale, J. D. MacKenzie and D. Richards, *Appl. Phys. Lett.*, 2001, **79**, 2178.
67 A. J. Cadby, R. Dean, C. Elliot, R. A. L. Jones, A. M. Fox and D. G. Lidzey, *Adv. Mater.*, 2007, **19**, 107.
68 A. Alexeev, J. Loos and M. M. Koetse, *Ultramicroscopy*, 2006, **106**, 191.
69 C. Groves, O. G. Reid and D. S. Ginger, *Acc. Chem. Res.*, 2010, **43**, 612.
70 R. Giridharagopal and D. S. Ginger, *J. Phys. Chem. Lett.*, 2010, **1**, 1160.
71 J. J. M. Halls, A. C. Arias, J. D. MacKenzie, W. Wu, M. Inbasekaran, E. P. Woo and R. H. Friend, *Adv. Mater.*, 2000, **12**, 498.
72 C. Yin, M. Schubert, S. Bange, B. Stiller, M. Castellani, D. Neher, M. Kumke and H.-H. Hörhold, *J. Phys. Chem. C*, 2008, **112**, 14607.
73 C. R. McNeill, H. Frohne, J. L. Holdsworth and P. C. Dastoor, *Nano Lett.*, 2004, **4**, 2503.
74 D. C. Coffey and D. S. Ginger, *Nat. Mater.*, 2006, **5**, 735.
75 C. R. McNeill, B. Watts, L. Thomsen, H. Ade, N. C. Greenham and P. C. Dastoor, *Macromolecules*, 2007, **40**, 3263.
76 C. R. McNeill, B. Watts, S. Swaraj, H. Ade, L. Thomsen, W. J. Belcher and P. C. Dastoor, *Nanotechnology*, 2008, **19**, 424015.
77 R. Q. Png, P. J. Chia, J. C. Tang, B. Liu, S. Sivaramakrishnan, M. Zhou, S. H. Khong, H. S. O. Chan, J. H. Burroughes, L. L. Chua, R. H. Friend and P. K. H. Ho, *Nat. Mater.*, 2009, **9**, 152.
78 T. J. K. Brenner and C. R. McNeill, *J. Phys. Chem. C*, 2011, **115**, 19364.
79 J. Loos, X. Yang, M. M. Koetse, J. Sweelssen, H. F. M. Schoo, S. C. Veenstra, W. Grogger, G. Kothleitner and F. Hofer, *J. Appl. Polym. Sci.*, 2005, **97**, 1001.
80 H. Yan, B. A. Collins, E. Gann, C. Wang, H. Ade and C. R. McNeill, *ACS Nano*, 2011, DOI: 10.1021/nn204150f, in press.
81 J. R. Moore, S. Albert-Seifried, A. Rao, S. Massip, B. Watts, D. J. Morgan, R. H. Friend, C. R. McNeill and H. Sirringhaus, *Adv. Energy Mater.*, 2011, **1**, 230.
82 W. Chen, T. Xu, F. He, W. Wang, C. Wang, J. Strzalka, Y. Liu, J. Wen, D. J. Miller, J. Chen, K. Hong, L. Yu and S. B. Darling, *Nano Lett.*, 2011, **11**, 3707.
83 B. P. Lyons, N. Clarke and C. Groves, *J. Phys. Chem. C*, 2011, **115**, 22572.
84 Y.-S. Huang, S. Westenhoff, I. Avilov, P. Sreearunothai, J. M. Hodgkiss, C. Deleener, R. H. Friend and D. Beljonne, *Nat. Mater.*, 2008, **7**, 483.
85 J.-L. Brédas, J. E. Norton, J. Cornil and V. Coropceanu, *Acc. Chem. Res.*, 2009, **42**, 1691.
86 H. Yan, S. Swaraj, C. Wang, I. Hwang, N. C. Greenham, C. Groves, H. Ade and C. R. McNeill, *Adv. Funct. Mater.*, 2010, **20**, 4329.
87 D. Chen, F. Liu, C. Wang, A. Nakahara and T. P. Russell, *Nano Lett.*, 2011, **11**, 2071.
88 N. D. Treat, M. A. Brady, G. Smith, M. F. Toney, E. J. Kramer, C. J. Hawker and M. L. Chabinyc, *Adv. Energy Mater.*, 2011, **1**, 82.
89 T. Kietzke, D. Neher, M. Kumke, R. Montenegro, K. Landfester and U. Scherf, *Macromolecules*, 2004, **37**, 4882.
90 T. Kietzke, D. Neher, K. Landfester, R. Montenegro, R. Guntner and U. Scherf, *Nat. Mater.*, 2003, **2**, 408.
91 K. B. Burke, A. J. Stapleton, B. Vaughan, X. Zhou, A. L. D. Kilcoyne, W. J. Belcher and P. C. Dastoor, *Nanotechnology*, 2011, **22**, 265710.
92 X. He, F. Gao, G. Tu, D. Hasko, S. Hüttner, U. Steiner, N. C. Greenham, R. H. Friend and W. T. S. Huck, *Nano Lett.*, 2010, **10**, 1302.
93 R. A. Segalman, B. McCulloch, S. Kirmayer and J. J. Urban, *Macromolecules*, 2009, **42**, 9205.
94 M. Sommer, S. Huettner and M. Thelakkat, *J. Mater. Chem.*, 2010, **20**, 10788.
95 P. D. Topham, A. J. Parnell and R. C. Hiorns, *J. Polym. Sci., Part B: Polym. Phys.*, 2011, **49**, 1131.
96 U. Scherf, S. Adamczyk, A. Gutacker and N. Koenen, *Macromol. Rapid Commun.*, 2009, **30**, 1059.
97 F. S. Bates, *Science*, 1991, **251**, 898.
98 B. D. Olsen and R. A. Segalman, *Mater. Sci. Eng., R*, 2008, **62**, 37.
99 R. Verduzco, I. Botiz, D. L. Pickel, S. M. Kilbey, K. Hong, E. Dimasi and S. B. Darling, *Macromolecules*, 2011, **44**, 530.
100 L. Bu, X. Guo, B. Yu, Y. Qu, Z. Xie, D. Yan, Y. Geng and F. Wang, *J. Am. Chem. Soc.*, 2009, **131**, 13242.
101 M. Sommer, S. Huttner, U. Steiner and M. Thelakkat, *Appl. Phys. Lett.*, 2009, **95**, 183308.